

Article

# Morphological Characterization and Effective Thermal Conductivity of Dual-Scale Reticulated Porous Structures

Simon Ackermann <sup>1</sup>, Jonathan R. Scheffe <sup>1</sup>, Jonas Duss <sup>1</sup> and Aldo Steinfeld <sup>1,2,\*</sup>

<sup>1</sup> Department of Mechanical and Process Engineering, ETH Zürich, Sonneggstrasse 3, 8092 Zürich, Switzerland; E-Mails: acsimon@ethz.ch (S.A.); jscheffe@ufl.edu (J.R.S.); jduss@student.ethz.ch (J.D.)

<sup>2</sup> Solar Technology Laboratory, Paul Scherrer Institute, 5232 Villigen PSI, Switzerland

\* Author to whom correspondence should be addressed; E-Mail: aldo.steinfeld@ethz.ch; Tel.: +41-44-6327929; Fax: +41-44-6321065.

External Editor: Javier Narciso

Received: 3 September 2014; in revised form: 13 October 2014 / Accepted: 15 October 2014 / Published: 28 October 2014

---

**Abstract:** Reticulated porous ceramic (RPC) made of ceria are promising structures used in solar thermochemical redox cycles for splitting CO<sub>2</sub> and H<sub>2</sub>O. They feature dual-scale porosity with mm-size pores for effective radiative heat transfer during reduction and µm-size pores within its struts for enhanced kinetics during oxidation. In this work, the detailed 3D digital representation of the complex dual-scale RPC is obtained using synchrotron submicrometer tomography and X-ray microtomography. Total and open porosity, pore size distribution, mean pore diameter, and specific surface area are extracted from the computer tomography (CT) scans. The 3D digital geometry is then applied in direct pore level simulations (DPLS) of Fourier’s law within the solid and the fluid phases for the accurate determination of the effective thermal conductivity at each porosity scale and combined, and for fluid-to-solid thermal conductivity from 10<sup>−5</sup> to 1. Results are compared to predictions by analytical models for structures with a wide range of porosities 0.09–0.9 in both the strut’s µm-scale and bulk’s mm-scale. The morphological properties and effective thermal conductivity determined in this work serve as an input to volume-averaged models for the design and optimization of solar chemical reactors.

**Keywords:** tomography; solar; thermochemical; conductivity; reticulated porous ceramic (RPC)

---

## 1. Introduction

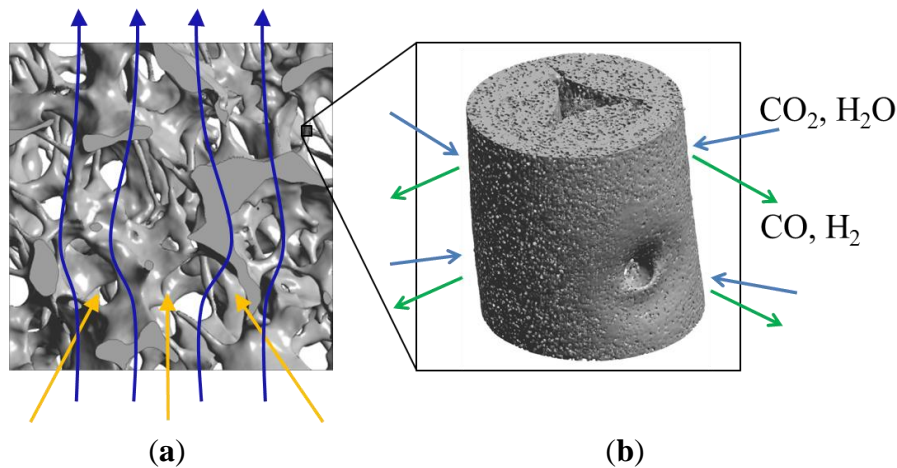
Foam-type reticulated porous ceramics (RPC) structures are applied in a broad range of physical processes requiring enhanced heat and mass transfer [1,2]. Applications include microelectronics cooling [3], soil dynamics [4,5], catalytic reactors [6], radiant burners [7], tissue engineering [3,8] and volumetric heat exchangers for the conversion of concentrated solar energy [9–11]. Of special interest of the latter application is the solar-driven thermochemical redox cycle for splitting  $\text{CO}_2$  and  $\text{H}_2\text{O}$  [12–16], consisting of: (1) a high-temperature endothermic reduction, in which a metal oxide is thermally reduced and oxygen is evolved; and (2) a lower-temperature exothermic oxidation, in which the reduced oxide is re-oxidized with  $\text{H}_2\text{O}$  and  $\text{CO}_2$  to form  $\text{H}_2$  and  $\text{CO}$  (syngas), and further processed to liquid hydrocarbon fuels. Ceria-based oxides have emerged as highly attractive redox materials because of the rapid oxygen transport in the bulk [14–18]. Various porous structures made of ceria have been investigated for enhanced reaction rates [18–20], including structures with submicron-sized interconnected pores, but these are problematic to retain because of partial sintering at elevated temperatures [19]. Furthermore, their high optical thickness inhibits penetration of concentrated solar radiation, resulting in non-uniform heating and temperature distributions [14]. Most recently, Furler *et al.* [15] presented a unique and morphologically stable RPC structure featuring dual-scale porosity: mm-size pores with struts containing micron-size pores. The mm-size pores enable volumetric absorption of concentrated solar radiation and effective heat transfer during the reduction step, while the micron-size pores within the struts offer increased specific surface area leading to enhanced reaction kinetics during the oxidation step.

Optimization of solar reactors for thermochemical redox cycles requires computational models of heat transfer and fluid dynamics coupled to the reaction kinetics [14,21]. Since resolving the solar reactor at the pore scale would require tremendous computational demand, volume-averaging theory is often applied for solving the mass, energy, and momentum conservation equations using effective heat and mass transport properties [22–25]. These can be determined accurately by direct pore-level simulations (DPLS) using the detailed 3D digital geometry of the structure obtained by computer tomography (CT) [26–28]. For example, the Monte Carlo ray-tracing method has been applied at the pore level for solving the radiative heat transfer equations and determining the effective extinction coefficient and scattering phase function [29], and the finite volume (FV) technique has been applied at the pore level for solving the Navier-Stokes equations and determining the effective thermal conductivity, permeability, and heat transfer coefficient [30,31].

In this work we apply the tomography-based methodology to investigate RPC structures made of ceria with dual-scale porosity in the mm and  $\mu\text{m}$  scales. This structure is schematically depicted in Figure 1 [15]. The total and open porosity, pore size distribution, mean pore diameter and specific surface area are extracted from the CT-scans. The effective thermal conductivity is determined by DPLS for the RPC with non-porous struts and for the RPC with dual-scale porosity. We investigate the effect that the dual-scale porosity has on the morphological properties and on the conduction heat

transfer across the RPC, and further compare the results to predictions by analytical models for structures with a wide range of porosities in both the strut's  $\mu\text{m}$ -scale and bulk's mm-scale.

**Figure 1.** Ceria RPC with dual-scale porosity: mm-size pores for volumetric radiative absorption and effective heat transfer (a) during the reduction step, and struts containing micron-sized pores leading to increased specific surface area (b) for enhanced reaction kinetics during the oxidation step.



## 2. Experimental

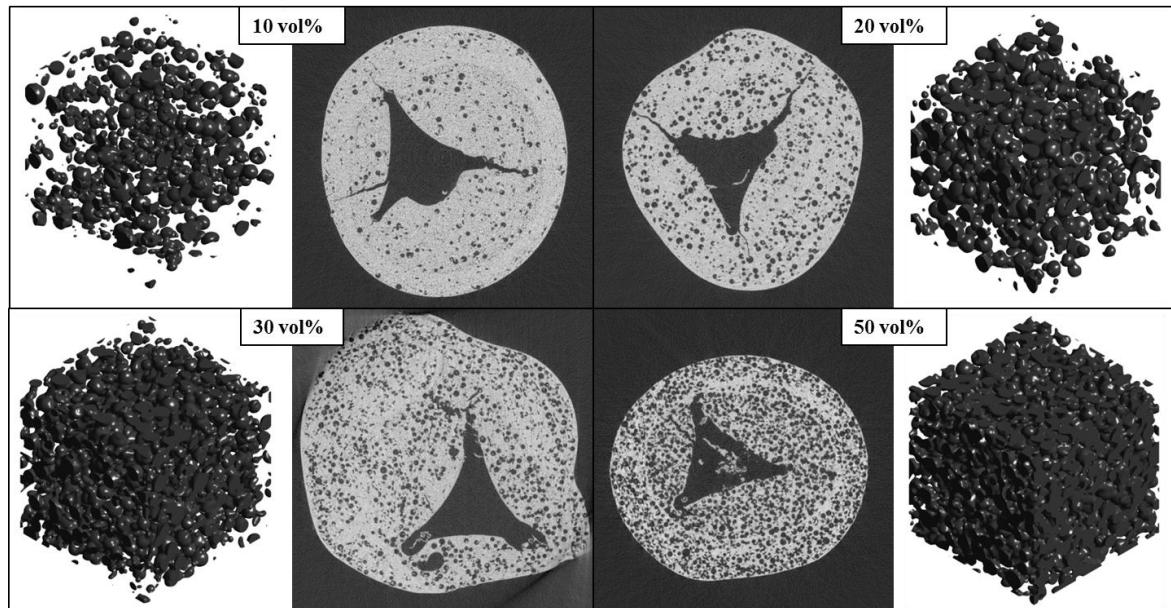
### 2.1. RPC Synthesis

The dual-scale RPC structure is manufactured using the Schwartzwalder foam replication method [32]. An organic foam template is coated with multiple slurry layers containing ceria particles and micron-sized carbon grains [15]. The carbon pore former content ranges from 10 to 50 vol%. After firing at high temperatures ( $>1800\text{ K}$ ), the bearing carbon foam and grains are burned and the desired foam-type structure undergoes sintering.

### 2.2. Synchrotron Submicrometer Tomography

Strut samples are scanned using synchrotron submicrometer tomography with a voxel (3D pixel) size of  $v_s = 325\text{ nm}$  and a  $0.832 \times 0.832 \times 0.702\text{ mm}^3$  field of view. The high-resolution CT is performed at the Swiss Light Source (SLS) of the Paul Scherrer Institute (PSI, Villigen, Switzerland) with the TOMCAT beamline for 40 keV photon energy, 400  $\mu\text{A}$  beam current, a 100  $\mu\text{m}$  thick aluminium filter, 40  $\mu\text{m}$  thick copper filter, a 10  $\mu\text{m}$  thick iron filter,  $20\times$  geometrical magnification, 1 s exposure time, 1001 projections. Figure 2 shows exemplary tomograms of strut samples manufactured with various concentrations of pore former ranging from 10 to 50 vol% and their corresponding 3D reconstructions of the pore space within isotropic strut regions. One tomogram contains  $2560 \times 2560$  pixels. Numerous strut samples are scanned to verify reproducibility.

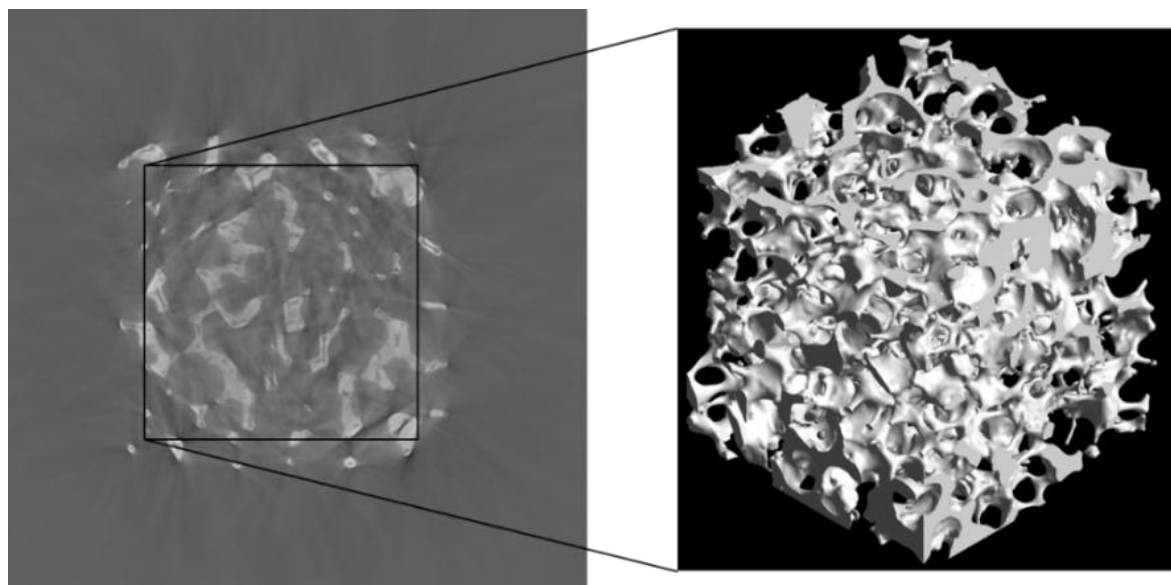
**Figure 2.** Synchrotron submicrometer computer tomograms of single RPC struts manufactured with various pore former concentrations (10, 20, 30, and 50 vol%) and their corresponding 3D digital reconstruction of the void space within isotropic porous strut region.



### 2.3. Micrometer Tomography

A ceria RPC sample with 10 pores per inch (ppi) is scanned by micrometer tomography with a voxel size of  $v_s = 35.7 \mu\text{m}$  and a  $36.56 \times 36.56 \times 36.56 \text{ mm}^3$  field of view. The low-resolution CT is performed with an unfiltered polychromatic X-ray beam at the Swiss Federal Laboratories for Materials Science and Technology (EMPA, Dübendorf, Switzerland) for 150 keV photon energy, 45  $\mu\text{A}$  beam current, 6.272 s exposure time and 721 projections. Figure 3 shows a tomogram and its corresponding 3D digital reconstruction of the scanned RPC sample. One tomogram contains  $1024 \times 1024$  pixels.

**Figure 3.** Computer tomogram of the RPC with mm-sized pores and 3D rendering of a cropped cubic sample.



### 3. Morphological Characterization

#### 3.1. Porosity

For the analysis of the strut structures, isotropic regions within submicrometer tomograms are cropped with the size of  $501 \times 501 \times 501$  voxels ( $0.163 \times 0.163 \times 0.163 \text{ mm}^3$ ). For the analysis of the RPC structures, micrometer tomograms are cropped to  $500 \times 500 \times 500$  voxels ( $17.85 \times 17.85 \times 17.85 \text{ mm}^3$ ). The cropped 8 bit tomograms obtained from measurements are pre-processed with a 3D Gaussian blurring filter to remove unwanted image noise derived from the photon sensor. Histograms computed from 3D tomogram stacks show bimodal character representing two grey scale pixel classes, with the threshold found by Otsu's method of intra-class variance minimization [33,34]. Finally, based on the threshold, each pixel is assigned to be either void or solid. Porosity,  $\varepsilon = V_f/V$ , is defined as the ratio between the void space volume and the total cube volume. It is calculated by counting void and solid voxels of the 3D stack. The representative elementary volume (REV) defines the minimum volume containing a porous zone for which the continuum assumption is valid. It is determined from incrementally growing cubic subvolumes until their calculated porosities convergences within a certain band,  $\pm\gamma$ . The conditions for the minimum edge length of the REV are [27]:

$$l_{\text{REV}} = \min \{L \leq L^* | \varepsilon - \gamma < \varepsilon(V_{L^*}) < \varepsilon + \gamma\}, \quad \gamma \ll 1 \quad (1)$$

where  $V_{L^*}$  is the sample subvolume and  $L^*$  is the edge length of the sample subvolume. For the RPC with a porosity band of  $\gamma = 0.05$ ,  $l_{\text{REV}} \geq 6.6 \text{ mm}$ , which leads to cube structures larger than 186 voxels edge length. For the  $\mu\text{m}$ -sized struts with a porosity band of  $\gamma = 0.05$ ,  $l_{\text{REV}} \geq 76.1 \text{ }\mu\text{m}$ , which leads to cube structures larger than 235 voxels edge length.

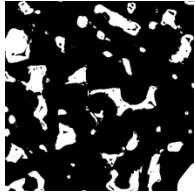
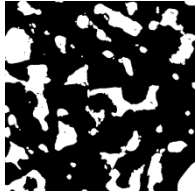
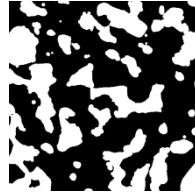

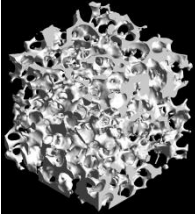
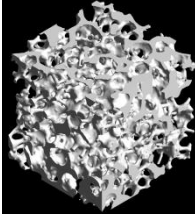
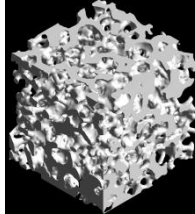
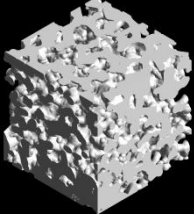
Dual-scale porosity,  $\varepsilon_{\text{dual}}$ , is calculated from strut-scale porosity,  $\varepsilon_{\text{strut}}$ , and RPC-scale porosity,  $\varepsilon_{\text{RPC}}$ , as:

$$\varepsilon_{\text{dual}} = \varepsilon_{\text{RPC}} + (1 - \varepsilon_{\text{RPC}}) \cdot \varepsilon_{\text{strut}} \quad (2)$$

$\varepsilon_{\text{strut}}$  is linearly fitted to the pore former concentration,  $\phi$ , as  $\varepsilon_{\text{strut}} = 0.008707 \phi$ . RPC structures with varying strut thicknesses are generated by altering the original segmented tomography scans through a dilation process with 3D spherical elements of a certain diameter,  $d$ , with  $\sqrt{\Delta x^2 + \Delta y^2 + \Delta z^2} \leq \frac{d}{2}$ . Table 1 lists the dilation radius, digital porosity, and mean pore diameter of the original RPC reconstruction and of the digitally altered RPC for 3 increasing strut thicknesses, and the corresponding digital section cut and 3D rendering. As expected, porosity and mean pore diameter of the RPC decrease with increasing strut dilation because the thicker struts consume void space.

Of special interest is the connectivity of the  $\mu\text{m}$ -sized pores within the struts. The pore connectivity scales directly with the specific surface area reachable by reacting gases, and thus scales with the fuel production rates [15]. Open porosity,  $\varepsilon_{\text{open}}$ , is defined as the pore space accessible from one of the 6 cube sample surfaces. An iterative routine starts searching from one cube side for connected neighbour void voxels in order to find all pores connected to this side. This reconstruction is performed to detect closed pores within the structure that account for the porosity but are not exposed to the gaseous reactants. Table 2 shows exemplary results of total and open porosity for strut samples with various pore former concentrations.

**Table 1.** Dilation radius, digital porosity, and mean pore diameter of the original RPC reconstruction and of the digitally altered RPC for increasing strut thickness, and the corresponding digital section cut and 3D rendering.

$r_{\text{dil}}$ (voxel)	0	2	5	10
$r_{\text{dil}}$ (mm)	0	0.071	0.179	0.357
$\epsilon_{\text{RPC}} (-)$	0.823	0.756	0.644	0.459
$d_{\text{mean}}$ (mm)	2.32	2.21	1.98	1.64
Digital section cut through 3D structure at $h = 50\%$				
3D rendering of RPC with mm-sized pores				

**Table 2.** Strut and open porosity, mean pore diameter, and the corresponding 3D rendering for strut samples manufactured with various pore former concentrations.

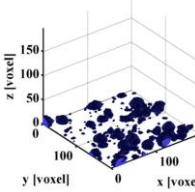
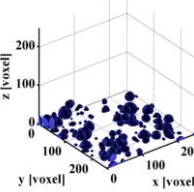
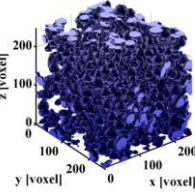
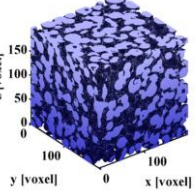
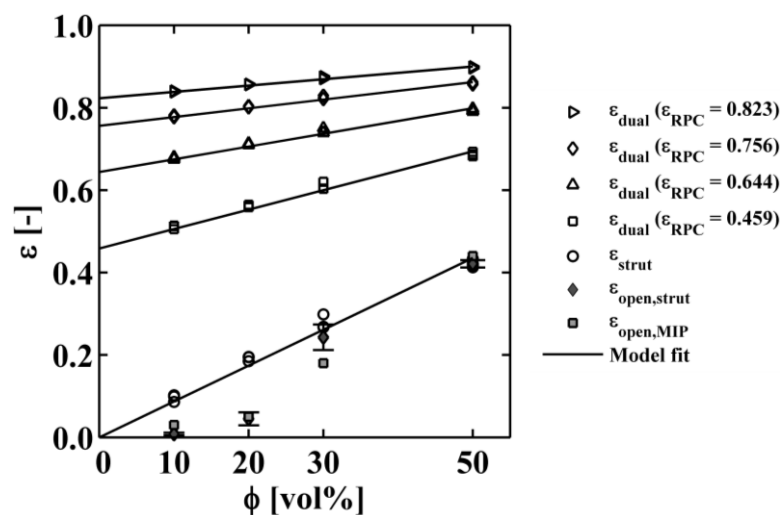
$\phi$ (vol%)	10	20	30	50
$\epsilon_{\text{strut}} (-)$	0.1195	0.1797	0.2605	0.4436
$\epsilon_{\text{open}} (-)$	0.0095	0.0102	0.2167	0.4423
$d_{\text{mean}}$ ( $\mu\text{m}$ )	9.22	11.50	9.62	9.12
3D rendering of connected pore space				

Figure 4 shows all results of the porosities collected from selected 3D tomography reconstructions.  $\epsilon_{\text{open}}$  is presented with error bars because 6 evaluations are obtained per sample (one from each side). For  $\phi \leq 20$  vol%, there is no pore connectivity observed as seen graphically in Table 2. For  $\phi \geq 30$  vol%, the majority of the pores are connected and the pore network passes through the entire cube sample. For 50 vol%, practically every pore is connected to the pore network since the open porosity and total porosity are almost the same  $\epsilon_{\text{open}} \approx \epsilon_{\text{strut}}$ . For high RPC porosity, e.g.,  $\epsilon_{\text{RPC}} = 0.825$ , the dual-scale porosity changes by less than 0.1 for  $\phi = 50$  vol% because only 17.5% of the volume is filled with  $\mu\text{m}$ -sized pores within the thin struts (see Figure 4). For lower RPC porosities, e.g.,  $\epsilon_{\text{RPC}} = 0.459$ , there is a stronger trend for increasing  $\phi$  since there is more solid to be filled with  $\mu\text{m}$ -sized pores. The porosities of the model fit for  $\phi = 0$  vol% represent  $\epsilon_{\text{RPC}}$  as listed in Table 1.

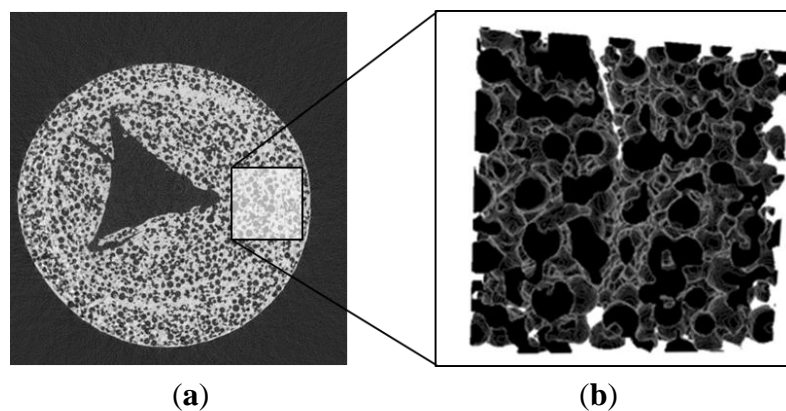
To investigate the transition from closed pores to interconnected pores in a systematic way, spheres with a small Gaussian size distribution of 2–3 voxels are randomly placed within the 3D volume. Pores of such artificially generated structures get connected between  $\epsilon_{\text{strut}} = 0.2$  and 0.3. Such connectivity

behavior is consistent with empirical correlations of the effective gas diffusivity within porous carbon [35]. Figure 4 also shows the comparison between the numerically determined  $\varepsilon_{\text{open}}$  and the experimentally measured values by mercury intrusion porosimetry (MIP) [36,37], as reported by Furler *et al.* [15]. The agreement is reasonable well. For  $\phi = 30$  vol%, the experimentally measured  $\varepsilon_{\text{open}}$  is lower than the numerically determined one due to poor pore connectivity across coating layers, as seen in Figure 5. This anisotropic region results from the 2-step coating applied during the fabrication process, and it is not considered in the determination of morphological properties and effective thermal conductivity within isotropic regions.

**Figure 4.** Total and open porosity as a function of the pore former concentration used to manufacture the  $\mu\text{m}$ -sized strut pores, total dual-scale porosity of RPC (original and digitally altered strut thickness).



**Figure 5.** Poor pore connectivity across fabrication layer originating from 2-step coating. (a) tomogram of a strut sample manufacture with 50 vol% carbon grain pore former. (b) 3D rendering of the void phase with pronounced solid barrier across the two coating layers.



### 3.2. Pore Size Distribution

Pore size distribution is determined by applying a morphology-altering algorithm to the digitally segmented 3D structure consisting of an inversion of the solid and void space, followed by erosion and



dilation with successively increasing spherical elements of diameter  $d$  with  $\sqrt{\Delta x^2 + \Delta y^2 + \Delta z^2} \leq \frac{d}{2}$ . In a last step, the algorithm inverts back the solid and void space. The cumulative pore size distribution  $1 - F(d)$  is defined as the ratio of the opening-closing porosity,  $\varepsilon_{oc}(d)$ , and the original porosity [27]:

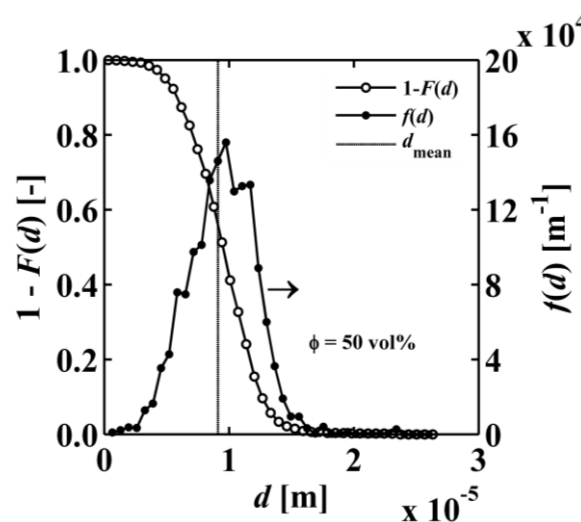
$$1 - F(d) = \frac{\varepsilon_{oc}(d)}{\varepsilon} \quad (3)$$

The pore size distribution is then calculated as:  $f(d) = dF(d)/dd$ . Figure 6 shows the cumulative pore size distribution (left y-axis) and pore size distribution (right y-axis) as a function of  $d$ .  $f(d)$  agrees qualitatively well with the values obtained by mercury intrusion porosimetry measurements. The mean pore diameter is then defined in such a way to split the area under the pore size distribution curve into two equal areas [27].

$$d_{\text{mean}} = \frac{\int_0^\infty d \cdot f(d) dd}{\int_0^\infty f(d) dd} \quad (4)$$

The mean pore diameter for porous strut samples with various concentrations of pore former in the range 10–50 vol% is listed in Table 2. As expected,  $d_{\text{mean}}$  remains independent of  $\phi$  at around 10  $\mu\text{m}$  because the same pore forming material is used to manufacture all samples.

**Figure 6.** Cumulative pore size distribution (**left** y-axis) and pore size distribution (**right** y-axis) obtained by morphology operations with spherical structuring elements of diameter  $d$ .



### 3.3. Specific Surface Area

The specific surface area (SSA) is determined in three different ways: (1) using statistical two-point correlation function computed on the 3D segmented structures with an in-house Fortran code; (2) resampling of the phase interface area with a surface mesh-based algorithm using the open source software ImageJ (version 1.47v, Java 1.6.0\_20 (64-bit)) [38] extended with the free BoneJ plugin (version 1.3.11) [39]; and (3) using the actual phase interface area of tetrahedral 3D meshes generated with an in-house Fortran code [40]. The in-house mesh generator covers the void and solid domain



with tetrahedral elements for unstructured body-fitted grids and subsequently refines the elements at the phase boundary. These 3D meshes are later used to solve the steady-state energy conservation equation to determine the effective thermal conductivity. The two point correlation  $s_2(r)$  is a statistical function that indicates the probability of two arbitrary points  $\Psi(r)$  and  $\Psi(\mathbf{r} + r\hat{\mathbf{s}})$  separated by the distance  $r$  to be in the void phase [41]:

$$s_2(r) = \frac{\int_V \int_{4\pi} \Psi(\mathbf{r}) \Psi(\mathbf{r} + r\hat{\mathbf{s}}) d\Omega dV}{4\pi V} \quad (5)$$

where  $\Omega$  is the solid angle and  $V$  the cube volume. Porosity and specific surface area are then calculated using the following expressions [27,30]:

$$s_2(r=0) = \varepsilon \quad (6)$$

$$s_2(r \rightarrow \infty) = \varepsilon^2 \quad (7)$$

$$\left. \frac{ds}{dr} \right|_{r=0} = -\frac{A_{0,2pc}}{4} \quad (8)$$

A code loops once through the entire structure ( $x$ -,  $y$ -,  $z$ -direction), counts each void voxel, and computes  $s_2(r=0)$  in a digitally exact manner. Additionally, the code counts for each void voxel the number of direct neighbour void voxels in all 6 directions ( $-x, x, -y, y, -z, z$ ) and computes  $s_2(r=1)$ . The volumetric specific surface area is then calculated as:

$$A_{0,2pc} = -4 \cdot \left. \frac{ds}{dr} \right|_{r=0} = \left| \frac{4}{v_s} [s_2(r=0) - s_2(r=1)] \right| \quad (9)$$

The specific surface area is presented in two different units: per total volume (fluid+solid phases),  $A_0$  [ $\text{m}^2 \cdot \text{m}^{-3}$ ], and per ceria mass,  $ssa$  [ $\text{m}^2 \cdot \text{g}^{-1}$ ]. The density of ceria is  $\rho_{\text{CeO}_2} = 7.22 \text{ g/cm}^3$  [21,42]. Dual-scale  $A_0$  is calculated by multiplying  $A_0$  determined for the struts by the solid volume fraction of the RPC:  $A_{0,\text{dual}} = (1 - \varepsilon_{\text{RPC}}) \cdot A_{0,\text{strut}}$ .  $A_0$  of RPC with non-porous struts is converted to  $ssa$  by:  $ssa_{\text{RPC}} = A_{0,\text{RPC}} / [(1 - \varepsilon_{\text{RPC}}) \cdot \rho_{\text{CeO}_2}]$ . Table 3 lists  $ssa$  of RPC with non-porous struts obtained from the original tomography scans and digitally dilated struts.

**Table 3.**  $ssa$  of RPC with non-porous struts obtained from tomography scans and digitally dilated struts.

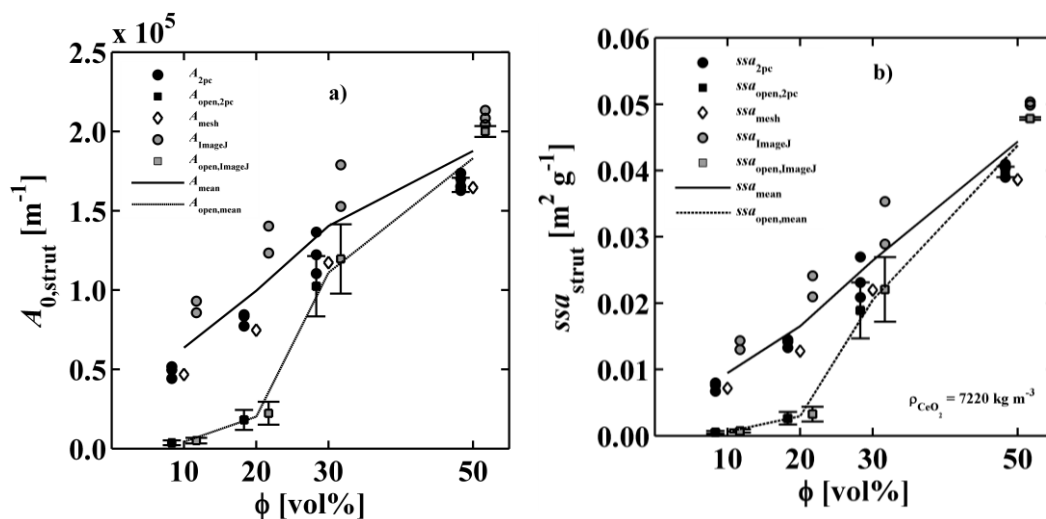
$r_{\text{dil}}$ (voxel)	0	2	5	10
$r_{\text{dil}}$ (mm)	0	0.071	0.179	0.357
$ssa_{\text{RPC},2pc}$ ( $\text{m}^2 \text{ g}^{-1}$ )	$9.06 \times 10^{-4}$	$5.89 \times 10^{-4}$	$4.07 \times 10^{-4}$	$2.62 \times 10^{-4}$
$ssa_{\text{RPC},\text{mesh}}$ ( $\text{m}^2 \text{ g}^{-1}$ )	$6.39 \times 10^{-4}$	$4.98 \times 10^{-4}$	$3.75 \times 10^{-4}$	$2.64 \times 10^{-4}$

Because  $ssa$  is defined per unit mass, the strut  $ssa$  is necessarily equal to the  $ssa$  of the entire structure, including mm and  $\mu\text{m}$  sized pores. Thus,  $A_{0,\text{strut}}$  is used to calculate  $ssa$  of porous struts and dual-scale porous structures:

$$ssa_{\text{strut}} = ssa_{\text{dual}} = \frac{A_{0,\text{strut}}}{(1 - \varepsilon_{\text{strut}}) \cdot \rho_{\text{CeO}_2}} \quad (10)$$

$A_0$  and  $ssa$  are plotted as a function of  $\phi$  in Figure 7a,b, respectively. Of special interest is the open  $ssa$ , which is directly related to the surface area reachable by the reacting gases for conversion of  $\text{CO}_2$  and  $\text{H}_2\text{O}$  to  $\text{CO}$  and  $\text{H}_2$ . The open  $ssa$  is calculated for the struts without closed pores. Open  $A_0$  and  $ssa$  are presented with error bars (standard deviation) for the data evaluated. Surface areas calculated from two-point correlation and phase interface area of the 3D meshes (black and white symbols) lie within close proximity to one another, whereas those calculated using ImageJ (grey symbols) are higher. This is because the two-point correlation is based on a statistical model leading to smoothing effects and the 3D meshes actually contain a smoothing algorithm for the phase interface, whereas the resampled phase interface of ImageJ incorporates fine mesh surface irregularities. For  $\phi \leq 20$  vol%, the open  $ssa$  is smaller than the total  $ssa$  because the majority of the pores are not connected. For  $\phi = 30$  vol% most pores are connected and the open  $ssa$  approaches the total  $ssa$ . For  $\phi = 50$  vol%, open and total  $ssa$  are nearly identical because at this point there are practically no closed pores (see Table 2). Trend lines are plotted defining the mean value of all different calculation methods for total (solid) and open (dashed)  $A_0$  and  $ssa$ .

**Figure 7.** Total and open specific surface area,  $ssa$ , as a function of the pore former concentration used to manufacture the  $\mu\text{m}$ -sized strut pores: (a) volumetric specific surface area of  $\mu\text{m}$ -sized strut pores; and (b) specific surface area per ceria mass of porous struts.



#### 4. Heat Conduction Modelling

The governing steady-state heat conduction equations within the solid phase and the stagnant fluid phase are given by:

$$\text{Solid phase: } \nabla(k_s \nabla T_s) = 0 \quad (11)$$

$$\text{Fluid phase: } \nabla(k_f \nabla T_f) = 0 \quad (12)$$

where  $k_s$  and  $k_f$  are the thermal conductivity of the solid and fluid, respectively. The cubic domain is schematically shown in Figure 8. The boundary conditions are given in Equations (13)–(17). An inlet and outlet temperature is set ( $T_{\text{hot}} > T_{\text{cold}}$ ) to provide a steady heat flux through the two phases with length  $L$ . Lateral walls of the sample cube are adiabatic. Local thermal equilibrium is assumed at the phase interface. Heat flux across the interface is driven by the temperature gradient and the thermal conductivities in each phase at the interface.

$$\text{Inlet temperature: } T_s(z=0) = T_f(z=0) = T_{\text{hot}} \quad (13)$$

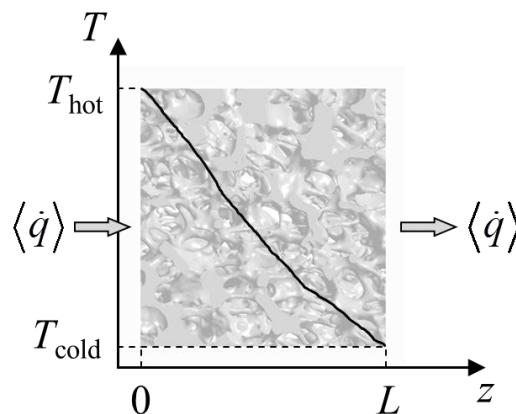
$$\text{Outlet temperature: } T_s(z=L) = T_f(z=L) = T_{\text{cold}} \quad (14)$$

$$\text{Adiabatic lateral walls: } \mathbf{n} \cdot \dot{\mathbf{q}} = 0 \quad (15)$$

$$\text{Local thermal equilibrium at phase interface: } T_s = T_f \quad (16)$$

$$\text{Heat flux across phase interface: } \mathbf{n} \cdot k_s \nabla T_s = \mathbf{n} \cdot k_f \nabla T_f \quad (17)$$

**Figure 8.** Schematic of the steady state heat conduction simulation setup with hot inlet temperature,  $T_{\text{hot}}$ , at  $z = 0$  and cold outlet temperature,  $T_{\text{cold}}$ , at  $z = L$ .



The governing volume-averaged steady-state equation for effective heat conduction within the isotropic porous structure reduces to one equation [22,23]:

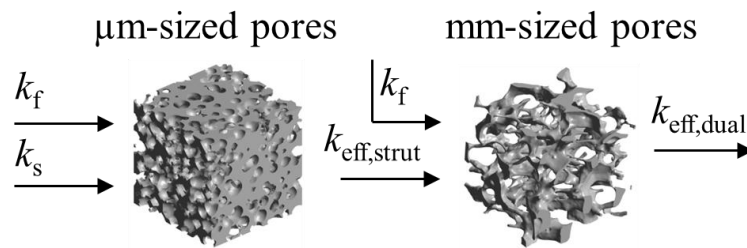
$$\nabla(k_{\text{eff}} \nabla \langle T \rangle) = 0 \quad (18)$$

The effective thermal conductivity is calculated using the 1D Fourier's law and the heat flux determined by DPLS:

$$k_{\text{eff}} \cdot A_{\text{flux}} \cdot \frac{T_{\text{hot}} - T_{\text{cold}}}{L} = \langle \dot{q} \rangle \quad (19)$$

where  $k_{\text{eff}}$  is the effective thermal conductivity of the cubic porous structure,  $\langle \dot{q} \rangle$  the effective heat flux at the inlet or outlet, and  $A_{\text{flux}} = L^2$  is the inlet or outlet area constraint with  $T_{\text{hot}}$  or  $T_{\text{cold}}$ , respectively. The methodology for determination of  $k_{\text{eff}}$  for dual-scale porous structures is schematically shown in Figure 9. In a first step,  $k_{\text{eff}}$  of the strut with  $\mu\text{m}$ -sized pores ( $k_{\text{eff, strut}}$ ) is determined according Equation (19). In a second step, this  $k_{\text{eff, strut}}$  serves as an input for the solid domain of a further simulation performed with the mm-sized pores of the RPC.

**Figure 9.** Methodology for the determination of the effective thermal conductivity of the RPC with dual-scale porosity.

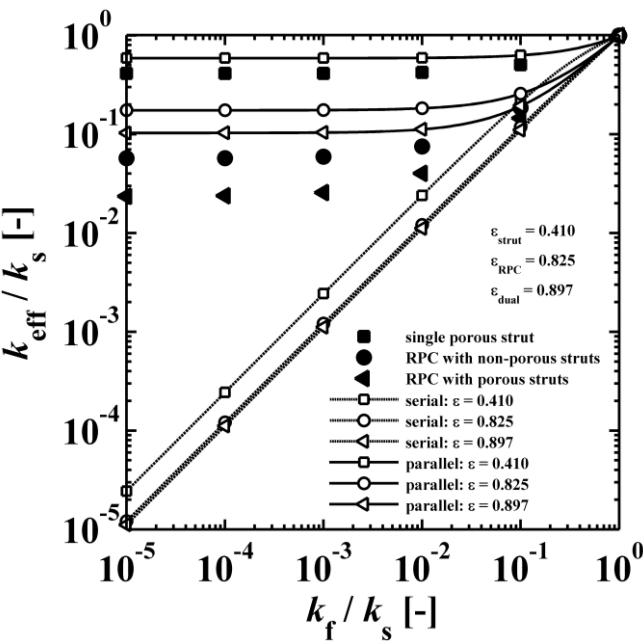


Numerical DPLS are performed for RPC with non-porous/porous struts with/without digital strut dilation for different fluid-solid thermal conductivity ratios ranging from  $10^{-5}$  up to 1. The cases covered include 4 RPC with non-porous struts (original scan and digitally dilated struts with 2, 5, and 10 voxels) and 16 RPC with porous struts (*i.e.*, 4 RPC, each with 4 different strut porosities  $\phi = 10, 20, 30, 50$  vol%). Simulations are performed using a commercial computational fluid dynamics (CFD) software (ANSYS® Academic Research, release 14.0). Initially, grid resolution study is performed, indicating convergence for structures containing element sizes between  $0.57 \mu\text{m}$  at fluid-solid interface to  $2.28 \mu\text{m}$  within bulk for the  $\mu\text{m}$ -size pores within the struts, and between  $62.0 \mu\text{m}$  at fluid-solid interface to  $247.9 \mu\text{m}$  within bulk for the mm-size pores of the RPC. Typical number of elements is 20 million, yielding an error of less than 1% compared to the finest mesh tested of 40 million. The correctness of the DPLS was verified by solving simple geometrical cases with exact analytical solutions, while its accuracy was fine-tuned by grid refinement.

Figure 10 shows the ratio of the effective thermal conductivity to the solid thermal conductivity *vs.* the ratio of the fluid-to-solid thermal conductivity for a single porous strut ( $\phi = 50$  vol%), a RPC with non-porous struts, and a RPC with porous struts ( $\phi = 50$  vol% and 0 mm strut dilation). The analytical curves for serial and parallel slabs are indicating the maximum and minimum possible heat flux [43,44]. These exemplary simulation results correspond to  $\varepsilon_{\text{strut}} = 0.410$  and  $\varepsilon_{\text{RPC}} = 0.825$ , leading to  $\varepsilon_{\text{dual}} = 0.897$ .  $k_{\text{eff}}$  decreases with increasing porosity and decreasing  $k_f/k_s$ . For  $k_f/k_s < 10^{-3}$ ,  $k_{\text{eff}}$  does not significantly change anymore, indicating heat conduction dominated by the solid domain (e.g., for vacuum applications). In that range, the ratio of  $k_{\text{eff}}$  for RPC with non-porous struts to  $k_{\text{eff}}$  for RPC with porous struts is 2.4. As expected, this ratio approaches 1 for increasing  $k_f/k_s$  as the thermal conductivities of the fluid and solid phases approach each other. The serial and parallel heat conduction mode of the lumped fluid and solid material bracket the minimum and maximum possible heat flux (also called Wiener lower and upper bound), respectively [43,44]. As expected, the simulation results (black symbols) are between the minimum (white symbols with dashed line) and maximum (white symbols with solid line) possible heat flux for each porosity.

Table 4 lists various analytical models for  $k_{\text{eff}}$  [31,45]. For simplicity, analytical equations are given in terms of  $\eta = k_f/k_s$ , and  $\varsigma_{\text{eff}} = k_{\text{eff}}/k_s$ . Several models allow fitting with geometrical shaping parameters. They were least-squares fitted to three different sets of simulation data: (1)  $k_{\text{eff,strut}}$  for a single porous strut (black squares shown in Figure 10); (2)  $k_{\text{eff,RPC}}$  for a RPC with non-porous struts (black circles shown in Figure 10); and (3)  $k_{\text{eff,dual}}$  for a RPC with porous struts (black triangles shown in Figure 10). To identify the model which agrees best with all data sets, an overall least-squares approximation,  $k_{\text{eff,all}}$ , was fitted for all simulation data.

**Figure 10.** Ratio of the effective thermal conductivity to the solid thermal conductivity vs. ratio of the fluid-to-solid thermal conductivity for a single porous strut ( $\phi = 50$  vol%), a RPC with non-porous struts, and a RPC with porous struts ( $\phi = 50$  vol%). The analytical curves for serial and parallel slabs are indicating the maximum and minimum possible heat flux.



**Table 4.** Analytical models for  $k_{eff}$ .

Model ID	Model	Analytical Expression $\left(\eta = \frac{k_f}{k_s}, \varsigma_{eff} = \frac{k_{eff}}{k_s}\right)$	Fitting Parameter
1	Parallel slabs [43,44,46]	$\varsigma_{eff} = \epsilon\eta + (1-\epsilon)$	None
2	Serial slabs [43,44,46]	$\varsigma_{eff} = \frac{\eta}{\epsilon + \eta(1-\epsilon)}$	None
3	Hashin and Shtrikman upper bound [47]	$\varsigma_{eff} = 1 + \frac{3(\eta-1)\epsilon}{3 + (\eta-1)(1-\epsilon)}$	None
4	Hashin and Shtrikman lower bound [47]	$\varsigma_{eff} = \eta + \frac{3\eta(1-\eta)(1-\epsilon)}{3\eta + (1-\eta)\epsilon}$	None
5	Woodside & Messmer [48]	$\varsigma_{eff} = \frac{1}{k_s} \cdot k_f^\epsilon \cdot k_s^{1-\epsilon} = \eta^\epsilon$	None
6	Russell [49]	$\varsigma_{eff} = \frac{\eta\epsilon^{2/3} + 1 - \epsilon^{2/3}}{\eta(\epsilon^{2/3} - \epsilon) + 1 - \epsilon^{2/3} + \epsilon}$	None
7	Loeb [50]	$\varsigma_{eff} = \frac{\epsilon^{1/3} - \epsilon + \eta(1 - \epsilon^{1/3} + \epsilon)}{\epsilon^{1/3} + \eta(1 - \epsilon^{1/3})}$	None
8	Maxwell model [45,51–53]	$\varsigma_{eff} = \frac{2 + \eta - 2\epsilon(1-\eta)}{2 + \eta + \epsilon(1-\eta)}$	None
9	Schuetz-Glicksmann [54,55]	$\varsigma_{eff} = \epsilon\eta + \frac{(1-\epsilon)}{3}$	None

Table 4. Cont.

Model ID	Model	Analytical Expression $\left(\eta = \frac{k_t}{k_s}, \zeta_{\text{eff}} = \frac{k_{\text{eff}}}{k_s}\right)$	Fitting Parameter
10	Bhattacharya <i>et al.</i> [56]	$\nu = \frac{-\sqrt{3}-2r+\sqrt{(\sqrt{3}+2r)^2+6\sqrt{3}(2\sqrt{3}r^2-4r+\sqrt{3})(1-\varepsilon)}}{2(2\sqrt{3}r^2-4r+\sqrt{3})}$ $\chi = 2r\nu$ $\zeta_a = \eta + (1-\eta)\left(\frac{1}{3} + \frac{2}{3}\nu - \frac{1}{6\sqrt{3}}\chi\right)$ $\zeta_b = \eta + \frac{1}{3}(1-\eta)(1+\chi)$ $\zeta_c = \eta + (1-\eta)\left(\frac{2}{3}\nu - \frac{2}{3\sqrt{3}}\chi\right)$ $\zeta_d = \eta + \frac{4}{3\sqrt{3}}(1-\eta)\chi$ $\zeta_{\text{eff}} = \left(\frac{2}{\sqrt{3}}\frac{\chi}{\zeta_a} + \frac{2}{\sqrt{3}}\frac{\sqrt{3}\nu - 2\chi}{\zeta_b} + \frac{2}{\sqrt{3}}\frac{\chi}{\zeta_c} + \frac{1-2\nu}{\zeta_d}\right)^{-1}$	$r$
11	Boomsma and Poulikakos [57]	$d = \sqrt{\frac{\sqrt{2}\left(2-\frac{5\sqrt{2}}{8}e^3-2\varepsilon\right)}{\pi(3-4\sqrt{2}e-e)}}$ $R_A = \frac{4d}{(2e^2+\pi d(1-e))(1-\eta)+4\eta}$ $R_B = \frac{(e-2d)^2}{e^2(e-2d)(1-\eta)+(2e-4d)\eta}$ $R_C = \frac{(\sqrt{2}-2e)^2}{2\pi d^2(1-2\sqrt{2}e)(1-\eta)+(2\sqrt{2}-4e)\eta}$ $R_D = \frac{2e}{e^2(1-\eta)+4\eta}$ $\zeta_{\text{eff}} = \frac{\sqrt{2}}{2(R_A + R_B + R_C + R_D)}$	$e$
12	Hamilton [58]	$\zeta_{\text{eff}} = \frac{\eta + n - 1 + (n-1)(\eta-1)\varepsilon}{\eta + n - 1 + (1-\eta)\varepsilon}$	$n$
13	Miller bound [59]	$\zeta_{\text{eff}} = \eta \left( 1 + (1-\varepsilon) \left( \frac{1}{\eta} - 1 \right) \right.$ $\left. - \frac{\frac{1}{3}\varepsilon(1-\varepsilon)\left(\frac{1}{\eta}-1\right)^2}{1 + \left(\frac{1}{\eta}-1\right)\left(1-\varepsilon + 3\left(\varepsilon^2 G_1 - (1-\varepsilon)^2 G_2\right)\right)} \right)$	$\frac{1}{9} \leq G_1 \leq \frac{1}{3}$ $\frac{1}{9} \leq G_2 \leq \frac{1}{3}$
14	Calmidi and Mahajan [60]	$\zeta_{\text{eff}} = \varepsilon\eta + A(1-\varepsilon)^n$	$A$ $n$
15	Dul'nev and Zarichnyak [22,30,61,62]	$\zeta_{\text{eff}} = (1-f)\frac{\eta}{\varepsilon + \eta(1-\varepsilon)} + f(\varepsilon\eta + 1 - \varepsilon)$	$f$
16	Extended three-resistor model (this work)	$f = c_0 + c_1\varepsilon + c_2\varepsilon^2$ $\zeta_{\text{eff}} = (1-f)\frac{\eta}{\varepsilon + \eta(1-\varepsilon)} + f(\varepsilon\eta + 1 - \varepsilon)$	$c_0$ $c_1$ $c_2$
17	Scalable three-resistor model (this work)	$\zeta_{\text{eff}} = c\varepsilon\frac{\eta}{b\varepsilon + \eta(1-b\varepsilon)} + (1-c\varepsilon)(a\varepsilon\eta + 1 - a\varepsilon)$	$a$ $b$ $c$

The root-mean-square error (RMS) is defined to compare  $k_{\text{eff}}$  calculated by the analytical models with that determined by our simulation:

$$\text{RMS} = 100\% \cdot \sqrt{\frac{1}{n} \sum_{i=1}^n \left( \log_{10} \left( \zeta_{\text{eff},i}^{\text{model}} \right) - \log_{10} \left( \zeta_{\text{eff},i}^{\text{simulation}} \right) \right)^2} \quad (20)$$

where  $n$  is the number of data points per data set over the entire range of  $k_{\text{eff}}/k_s$  and  $k_f/k_s$  indicated in Figure 10. Table 5 lists the RMS for the three different simulation data sets and for  $k_{\text{eff,all}}$ . Only those models giving an RMS < 5% are considered appropriate. Models 1 to 9, which are not using any geometrical shaping parameter, give RMS > 10%. However, some models perform comparatively well for the prediction of  $k_{\text{eff,strut}}$  with a RMS < 5%: Hashin and Shtrikman upper bound [47] (3.0%), Russell [49] (4.8%), Loeb [50] (2.6%) and Maxwell [51] (3.0%) which is consistent with the findings by Petrasch *et al.* [31] for SiC foams. Serial slab and Hashin and Shtrikman lower bound give very inaccurate predictions of  $k_{\text{eff}}$  (RMS > 200%). This is because the serial bound model assumes no direct connection of solid paths between heat inlet and outlet area, which is obviously not the case for connected, but tortuous strut paths. The Schuetz-Glicksmann model [54,55] yields inaccurate results (21.6%) and predicts values out of the range of the Wiener lower and upper bounds for  $k_f/k_s > 0.33$ . The fitted model of Bhattacharya *et al.* [56] can accurately predict  $k_{\text{eff,strut}}$  (1.5%). However, for the other simulation data sets, RMS > 10%. The model of Boomsma and Poulikakos [57] cannot be applied. Model is not suitable because equations lead to negative length scales in section B (one of four resistances) for any porosity and fitting parameter combination, geometrically describing a non-physical difference between the half node side length and the ligament radius. The fitted model of Hamilton *et al.* [58] gives only  $k_{\text{eff,strut}}$  with RMS < 5%. The fitted Miller's bound [59] model, shown in Figure 11a, accurately represents the simulation results for  $k_{\text{eff,strut}}$  (0.4%),  $k_{\text{eff,RPC}}$  (1.8%),  $k_{\text{eff,dual}}$  (2.1%) and  $k_{\text{eff,all}}$  (1.9%). This model assumes statistical bound for two-phase media and uses two fitting parameters,  $G_1$  and  $G_2$ , including spherical (number  $\frac{1}{9}$ ) up to platelike (number  $\frac{1}{3}$ ) void and solid shapes. Miller's bound model is restricted within the upper and lower bound of Hashin and Shtrikman [59] for all fitting parameters. The empirical model of Calmidi and Mahajan [60], shown in Figure 11b, is capable of predicting all three data sets and an overall data sets with a RMS < 5%. The model of Dul'nev and Zarichnyak [62] gives only  $k_{\text{eff,strut}}$  with a RMS < 5%. Dul'nev and Zarichnyak [22,30,61,62] propose a model using a linear combination of the Wiener lower and upper bounds with empirical fitting parameter,  $f$ , for weighting linear combination which is also called three-resistor model. However, if  $k_{\text{eff}}$  is fitted individually for each structure (porosity), an inverse trend of  $f$  is observed with porosity. Therefore, the three-resistor model is then extended by describing  $f$  as a 2nd-order polynomial function with porosity. Such extended three-resistor model, shown in Figure 11c, predicts  $k_{\text{eff,strut}}$  with RMS = 0.3% instead of 3.9%,  $k_{\text{eff,RPC}}$  with RMS = 1.6% instead of 9.2%,  $k_{\text{eff,dual}}$  with RMS = 2.2% instead of 9.8%, and  $k_{\text{eff,all}}$  with RMS = 2.3% instead of 12.6%. The three fitting parameters describing  $f$  with a 2nd-order polynomial function ( $c_0, c_1, c_2$ ) are replaced to allow the serial and parallel resistance, as well as their combination, to linearly scale with porosity, as shown schematically in Figure 12. Least-squares fitting of this modified three-resistor model, shown in Figure 11d, delivers the most accurate predictions:  $k_{\text{eff,strut}}$  with RMS = 0.1%,  $k_{\text{eff,RPC}}$  with RMS = 1.1%,  $k_{\text{eff,dual}}$  with RMS = 1.4%, and  $k_{\text{eff,all}}$  with RMS = 1.3%. The modified three-resistor



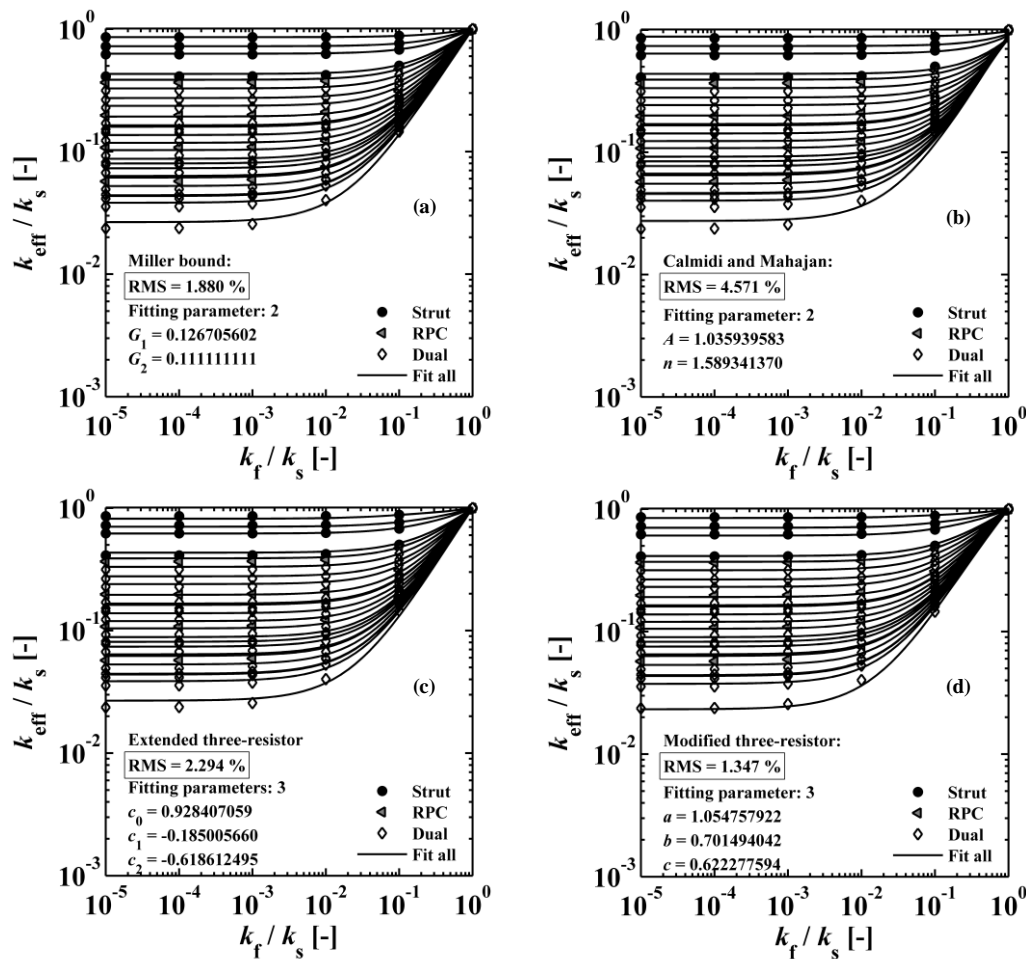
model shows the best performance in prediction of  $k_{\text{eff}}$  with overall RMS < 1.5%. Fitting parameter  $a$  and  $b$  allow the lumped fluid and solid parts to deviate from actual  $\varepsilon$  within the parallel and serial slabs, respectively. Fitting parameter  $c$  allows linear combination of the serial and parallel slab to deviate from  $\varepsilon$ . This gives some degree of freedom for capturing different tortuous regions for a high porosity range ( $0.09 < \varepsilon < 0.9$ ) and predicts the effective thermal conductivity more accurately compared to linear (or non-linear) combination of parallel/serial bounds and to Miller's bound model.

**Table 5.** Root-mean-square (RMS) error of analytical models compared to three simulation data sets and to all simulation data.

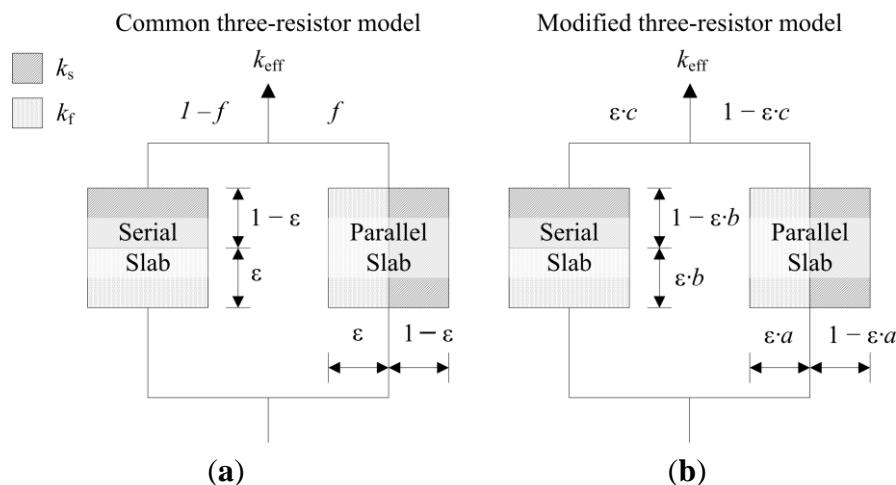
Model	RMS	$k_{\text{eff, strut}} (n = 24)$	$k_{\text{eff, RPC}} (n = 24)$	$k_{\text{eff, dual}} (n = 96)$	$k_{\text{eff, all}} (n = 144)$
1	RMS (%)	7.516	26.861	32.158	28.620
2	RMS (%)	233.780	223.485	213.144	218.449
3	RMS (%)	3.010	16.561	20.992	18.466
4	RMS (%)	204.379	207.200	200.080	202.003
5	RMS (%)	63.012	139.992	148.175	136.255
6	RMS (%)	4.772	17.828	22.024	19.497
7	RMS (%)	2.611	15.241	19.916	17.443
8	RMS (%)	3.010	16.561	20.992	18.466
9	RMS (%)	7.516	26.861	32.158	21.621
10	$r$	0.2912	0.1972	0.1254	0.2684
	RMS (%)	1.484	10.738	5.829	13.102
11	RMS (%)	N/A <sup>1</sup>	N/A <sup>1</sup>	N/A <sup>1</sup>	N/A <sup>1</sup>
12	$n$	2.1985	1.6343	1.5325	1.5701
	RMS (%)	1.247	5.822	6.984	6.868
13	$G_1$	1/9	0.1262	0.1268	0.1267
	$G_2$	0.1430	1/9	1/9	1/9
	RMS (%)	0.409	1.828	2.071	1.880
14	$A$	1.0285	1.0482	1.0709	1.0360
	$n$	1.6083	1.5990	1.6095	1.5893
	RMS (%)	2.217	4.721	4.933	4.571
15	$f$	0.8377	0.4954	0.4217	0.4865
	RMS (%)	3.945	9.164	9.754	12.595
16	$c_0$	0.9972	0.3336	0.2581	0.9284
	$c_1$	−0.4634	1.6570	1.6780	−0.1850
	$c_2$	−0.5544	−1.9954	−1.8817	−0.6186
	RMS (%)	0.261	1.611	2.202	2.294
17	$a$	1.3194	1.0823	1.0541	1.0548
	$b$	0.3181	0.6475	0.7008	0.7015
	$c$	0.2000	0.5444	0.6229	0.6223
	RMS (%)	0.135	1.057	1.373	1.347

<sup>1</sup> Model is not suitable because equations lead to negative length scales in section B (one of four resistances) for any porosity and fitting parameter combination, geometrically describing a non-physical difference between the half node side length and the ligament radius.

**Figure 11.** Ratio of the effective thermal conductivity to the solid thermal conductivity vs. ratio of the fluid-to-solid thermal conductivity, obtained by our simulation and by least-squares fitted models for structures with a high range of porosities ( $0.09 < \varepsilon < 0.9$ ). Shown are: (a) Miller bound model [59]; (b) Calmidi and Mahajan model [60]; (c) extended three-resistor model; and (d) modified three-resistor model. The modified three-resistor model predicts  $k_{\text{eff}}$  with the lowest RMS.



**Figure 12.** (a) Common three-resistor model [22]; (b) modified three-resistor model with scaling parameter for the serial and parallel slab and their combination.



## 5. Summary and Conclusions

High and low resolution computer tomographic scans were performed on complex reticulated porous ceramics (RPC) structures to capture the 3D digital representations of their dual-scale porosity in the mm and  $\mu\text{m}$  range. The CT scans were processed with a Gaussian blurring filter for a clustering-based image thresholding of the void and solid phases using Otsu's method. The struts containing  $\mu\text{m}$ -size pores were digitally dilated with spherical structuring elements generating structures with different thickness and porosity. The morphological properties analyzed include porosity, pore size distribution, specific surface area, and pore connectivity within representative sample volumes of the isotropic strut regions and of the RPC. The total strut porosity was linearly dependent on the concentration of pore forming agent, and no pore connectivity was observed for concentration less than 20 vol%, consistent with mercury intrusion porosimetry measurements. A well-connected pore network results in high specific surface area and penetration of reactant gas for high fuel production. The effective thermal conductivities of a single porous strut, a RPC with non-porous struts, and a RPC with porous struts (dual scale) were determined by direct pore level simulations of the heat conduction equation with a CFD code. Values were compared to predictions by analytical models over a wide range of porosities. Models without shaping parameters were generally inaccurate (overall RMS > 10%). Miller's model with two shaping parameters predicted  $k_{\text{eff}}$  with RMS error below 2.1% and the modified three-resistor model with three empirical fitting parameters predicted  $k_{\text{eff}}$  with a RMS error below 1.5%. These analytical correlations are applicable to RPC with porosities in both the strut's  $\mu\text{m}$ -scale and bulk's mm-scale ranging from 0.09 to 0.9.

The morphological properties and effective thermal conductivity determined in this work serve as an input to volume-averaged models for the design and optimization of solar chemical reactors.

## Acknowledgments

We gratefully acknowledge the financial support by the Swiss Competence Center Energy & Mobility, the Helmholtz–Gemeinschaft Deutscher Forschungszentren (Virtuelles Institut SolarSyngas), and the European Research Council under the European Union's ERC Advanced Grant (SUNFUELS—No. 320541).

## Nomenclature

$A_{0,(.)}$	Volumetric specific surface area ( $\text{m}^{-1}$ )
$A_{\text{flux}}$	Cross sectional inlet/outlet area of cubic sample for heat flux ( $\text{m}^2$ )
$ssa_{(.)}$	Physical specific surface area (Index: strut, RPC, dual) ( $\text{m}^2 \text{ g}^{-1}$ )
$d$	Diameter of spherical structuring elements (m)
$d_{\text{mean}}$	Mean pore diameter (m)
$f(d)$	Pore size distribution (—)
$F(d)$	Cumulative pore size distribution (—)
$k_s$	Solid thermal conductivity ( $\text{W m}^{-1} \text{ K}^{-1}$ )
$k_f$	Fluid thermal conductivity ( $\text{W m}^{-1} \text{ K}^{-1}$ )
$k_{\text{eff},(.)}$	Effective thermal conductivity of porous structure ( $\text{W m}^{-1} \text{ K}^{-1}$ )

$l_{REV}$	Cube edge length of representative elementary volume (m)
$L$	Cube edge length (m)
$n$	Number of simulation data points (–)
$\dot{q}$	Heat flux through sample ( $\text{W m}^{-2}$ )
$s_2(r)$	Two point correlation function (–)
$T_{\text{cold}}$	Cold side temperature (K)
$T_f$	Fluid temperature (K)
$T_{\text{hot}}$	Hot side temperature (K)
$T_s$	Solid temperature (K)
$v_s$	Voxel size (m)
$V$	Total sample cube volume ( $\text{m}^3$ )
$V_f$	Void volume ( $\text{m}^3$ )
$\varepsilon(.)$	Porosity (–)
$\gamma$	Error band of porosity (–)
$\zeta_{\text{eff}}$	Ratio of effective to solid thermal conductivity (–)
$\eta$	Ratio of fluid to solid thermal conductivity (–)
$\phi$	Pore former concentration (vol%)

## Subscripts

2pc	2-point correlation
mesh	3D-mesh generated from digitally segmented structures
ImageJ	Calculated using open source software ImageJ
strut	Morphological property of porous strut
RPC	Morphological property of RPC with non-porous struts
dual	Morphological property of RPC with porous struts (dual-scale)
open	Open morphological property excluding closed pores
oc	Morphological property after applying opening-closing algorithm

## Conflicts of Interest

The authors declare no conflict of interest.

## References

1. Bear, J.; Buchlin, J.M. *Modelling and Applications of Transport Phenomena in Porous Media*; Kluwer Academic Publishers: Dordrecht, The Netherlands, 1991; p. 380.
2. Ho, C.K.; Webb, S.W. *Gas Transport in Porous Media*; Springer: Dordrecht, The Netherlands, 2006; p. 44.
3. Vadász, P.T. *Emerging Topics in Heat and Mass Transfer in Porous Media: From Bioengineering and Microelectronics to Nanotechnology*; Springer: Dordrecht, The Netherlands, 2008; p. 328.
4. Verruijt, A. *An Introduction to Soil Dynamics*; Springer: Dordrecht, The Netherlands, 2010; p. 433.

5. Bear, J.; Verruijt, A. *Modeling Groundwater Flow and Pollution: With Computer Programs for Sample Cases*; D. Reidel Pub. Co.: Dordrecht, The Netherlands, 1987; p. 414.
6. Dhamrat, R.S.; Ellzey, J.L. Numerical and experimental study of the conversion of methane to hydrogen in a porous media reactor. *Combust. Flame* **2006**, *144*, 698–709.
7. Pantangi, V.K.; Mishra, S.C.; Muthukumar, P.; Reddy, R. Studies on porous radiant burners for lpg (liquefied petroleum gas) cooking applications. *Energy* **2011**, *36*, 6074–6080.
8. Zermatten, E.; Vetsch, J.R.; Ruffoni, D.; Hofmann, S.; Müller, R.; Steinfeld, A. Micro-computed tomography based computational fluid dynamics for the determination of shear stresses in scaffolds within a perfusion bioreactor. *Ann. Biomed. Eng.* **2014**, *42*, 1085–1094.
9. Fend, T.; Hoffschmidt, B.; Pitz-Paal, R.; Reutter, O.; Rietbrock, P. Porous materials as open volumetric solar receivers: Experimental determination of thermophysical and heat transfer properties. *Energy* **2004**, *29*, 823–833.
10. Hischier, I.; Leumann, P.; Steinfeld, A. Experimental and numerical analyses of a pressurized air receiver for solar-driven gas turbines. *J. Sol. Energy Eng.* **2012**, *134*, 1–8.
11. Hischier, I.; Poživil, P.; Steinfeld, A. A modular ceramic cavity-receiver for high-temperature high-concentration solar applications. *J. Sol. Energy Eng.* **2011**, *134*, doi:10.1115/1.4005107.
12. Romero, M.; Steinfeld, A. Concentrating solar thermal power and thermochemical fuels. *Energy Environ. Sci.* **2012**, *5*, 9234–9245.
13. Miller, J.E.; McDaniel, A.H.; Allendorf, M.D. Considerations in the design of materials for solar-driven fuel production using metal-oxide thermochemical cycles. *Adv. Energy Mater.* **2014**, *4*, doi:10.1002/aenm.201300469.
14. Furler, P.; Scheffe, J.; Gorbar, M.; Moes, L.; Vogt, U.; Steinfeld, A. Solar thermochemical CO<sub>2</sub> splitting utilizing a reticulated porous ceria redox system. *Energy Fuels* **2012**, *26*, 7051–7059.
15. Furler, P.; Scheffe, J.; Marxer, D.; Gorbar, M.; Bonk, A.; Vogt, U.; Steinfeld, A. Thermochemical CO<sub>2</sub> splitting via redox cycling of ceria reticulated foam structures with dual-scale porosities. *PCCP* **2014**, *16*, 10503–10511.
16. Furler, P.; Scheffe, J.R.; Steinfeld, A. Syngas production by simultaneous splitting of H<sub>2</sub>O and CO<sub>2</sub> via ceria redox reactions in a high-temperature solar reactor. *Energy Environ. Sci.* **2012**, *5*, 6098–6103.
17. Ackermann, S.; Scheffe, J.R.; Steinfeld, A. Diffusion of oxygen in ceria at elevated temperatures and its application to H<sub>2</sub>O/CO<sub>2</sub> splitting thermochemical redox cycles. *J. Phys. Chem. C* **2014**, *118*, 5216–5225.
18. Chueh, W.C.; Falter, C.; Abbott, M.; Scipio, D.; Furler, P.; Haile, S.M.; Steinfeld, A. High-flux solar-driven thermochemical dissociation of CO<sub>2</sub> and H<sub>2</sub>O using nonstoichiometric ceria. *Science* **2010**, *330*, 1797–1801.
19. Venstrom, L.J.; Petkovich, N.; Rudisill, S.; Stein, A.; Davidson, J.H. The effects of morphology on the oxidation of ceria by water and carbon dioxide. *J. Sol. Energy Eng.* **2012**, *134*, doi:10.1115/1.4005119.
20. Gibbons, W.T.; Venstrom, L.J.; de Smith, R.M.; Davidson, J.H.; Jackson, G.S. Ceria-based electrospun fibers for renewable fuel production via two-step thermal redox cycles for carbon dioxide splitting. *Phys. Chem. Chem. Phys.* **2014**, *16*, 14271–14280.

21. Keene, D.J.; Davidson, J.H.; Lipiński, W. A model of transient heat and mass transfer in a heterogeneous medium of ceria undergoing nonstoichiometric reduction. *J. Heat Transfer* **2013**, *135*, doi:10.1115/1.4023494.
22. Kaviany, M. *Principles of Heat Transfer in Porous Media*, 2nd ed.; Springer-Verlag: New York, NY, USA, 1995; p. 708.
23. Whitaker, S. *The Method of Volume Averaging*; Series: Theory and Applications of Transport in Porous Media); Kluwer Academic: Dordrecht, The Netherlands, 1999; p. 219.
24. Bodla, K.K.; Weibel, J.A.; Garimella, S.V. Advances in fluid and thermal transport property analysis and design of sintered porous wick microstructures. *J. Heat Transf.* **2013**, *135*, doi:10.1115/1.4023569.
25. Krishnan, S.; Murthy, J.Y.; Garimella, S.V. Direct simulation of transport in open-cell metal foam. *J. Heat Transf.* **2006**, *128*, 793–799.
26. Petrasch, J.; Meier, F.; Friess, H.; Steinfeld, A. Tomography based determination of permeability, dupuit-forchheimer coefficient, and interfacial heat transfer coefficient in reticulate porous ceramics. **2008**, *29*, 315–326.
27. Petrasch, J.; Wyss, P.; Stämpfli, R.; Steinfeld, A. Tomography-based multiscale analyses of the 3D geometrical morphology of reticulated porous ceramics. *J. Am. Ceram. Soc.* **2008**, *91*, 2659–2665.
28. Bodla, K.K.; Murthy, J.Y.; Garimella, S.V. Microtomography-based simulation of transport through open-cell metal foams. *Numer. Heat Transf. A Appl.* **2010**, *58*, 527–544.
29. Petrasch, J.; Wyss, P.; Steinfeld, A. Tomography-based monte carlo determination of radiative properties of reticulate porous ceramics. *J. Quant. Spectrosc. Radiat. Transf.* **2007**, *105*, 180–197.
30. Haussener, S.; Coray, P.; Lipinski, W.; Wyss, P.; Steinfeld, A. Tomography-based heat and mass transfer characterization of reticulate porous ceramics for high-temperature processing. *J. Heat Transf.* **2010**, *132*, doi:10.1115/1.4000226.
31. Petrasch, J.; Schrader, B.; Wyss, P.; Steinfeld, A. Tomography-based determination of the effective thermal conductivity of fluid-saturated reticulate porous ceramics. *ASME J. Heat Transf.* **2008**, *130*, doi:10.1115/1.2804932.
32. Karl, S.; Somers, A.V. Method of Making Porous Ceramic Articles. U.S. Patent 3090094 A, 21 May 1963.
33. Otsu, N. A threshold selection method from gray-level histograms. *IEEE Trans. Syst. Man Cybern.* **1979**, *9*, 62–66.
34. Sezgin, M.; Sankur, B.L. Survey over image thresholding techniques and quantitative performance evaluation. *ELECTIM* **2004**, *13*, 146–168.
35. Zamel, N.; Li, X.; Shen, J. Correlation for the effective gas diffusion coefficient in carbon paper diffusion media. *Energy Fuels* **2009**, *23*, 6070–6078.
36. Giesche, H. Mercury porosimetry: A general (practical) overview. *Part. Part. Syst. Charact.* **2006**, *23*, 9–19.
37. Webb, P.A. *An Introduction to the Physical Characterization of Materials by Mercury Intrusion Porosimetry with Emphasis on Reduction and Presentation of Experimental Data*; Micromeritics Instrument Corp.: Norcross, GA, USA, 2001.

38. Abramoff, M.D.; Magalhães, P.J.; Ram, S.J. Image processing with imageJ. *Biophoton. Int.* **2004**, *11*, 36–43.
39. Doube, M.; Klosowski, M.M.; Arganda-Carreras, I.; Cordelières, F.P.; Dougherty, R.P.; Jackson, J.S.; Schmid, B.; Hutchinson, J.R.; Shefelbine, S.J. BoneJ: Free and extensible bone image analysis in imageJ. *Bone* **2010**, *47*, 1076–1079.
40. Friess, H.; Haussener, S.; Steinfeld, A.; Petrasch, J. Tetrahedral mesh generation based on space indicator functions. *Int. J. Numer. Methods Eng.* **2013**, *93*, 1040–1056.
41. Berryman, J.G.; Blair, S.C. Use of digital image analysis to estimate fluid permeability of porous materials: Application of two-point correlation functions. *J. Appl. Phys.* **1986**, *60*, 1930–1938.
42. Mogensen, M.; Sammes, N.M.; Tompsett, G.A. Physical, chemical and electrochemical properties of pure and doped ceria. *Solid State Ion.* **2000**, *129*, 63–94.
43. Bruggeman, D.A.G. Berechnung verschiedener physikalischer konstanten von heterogenen substanzen. I. Dielektrizitätskonstanten und leitfähigkeiten der mischkörper aus isotropen substanzen. *Ann. Phys.* **1935**, *416*, 636–664. (In German)
44. Deissler, R.G.; Boegli, J.S. An investigation of effective thermal conductivities of powders in various gases. *Trans. ASME* **1958**, *80*, 1417–1425.
45. Wang, M.; Pan, N. Predictions of effective physical properties of complex multiphase materials. *Mater. Sci. Eng. R Rep.* **2008**, *63*, 1–30.
46. DeVera, A.L.; Strieder, W. Upper and lower bounds on the thermal conductivity of a random, two-phase material. *J. Phys. Chem.* **1977**, *81*, 1783–1790.
47. Hashin, Z.; Shtrikman, S. A variational approach to the theory of the effective magnetic permeability of multiphase materials. *J. Appl. Phys.* **1962**, *33*, 3125–3131.
48. Woodside, W.; Messmer, J.H. Thermal conductivity of porous media. II. Consolidated rocks. *J. Appl. Phys.* **1961**, *32*, 1699–1706.
49. Russell, H.W. Principles of heat flow in porous insulators. *J. Am. Ceram. Soc.* **1935**, *18*, 1–5.
50. Loeb, A.L. Thermal conductivity: VIII, a theory of thermal conductivity of porous materials. *J. Am. Ceram. Soc.* **1954**, *37*, 96–99.
51. Maxwell, J.C. *A Treatise on Electricity and Magnetism*, 3rd ed.; Dover Publications: New York, NY, USA, 1954.
52. Choy, T.C. *Effective Medium Theory: Principles and Applications*; Oxford University Press: Oxford, UK, 1999; p. 182.
53. Sattler, K.D. *Handbook of Nanophysics. Nanoparticles and Quantum Dots*; Taylor & Francis: Boca Raton, FL, USA, 2011.
54. Kamiuto, K. Modeling of composite heat transfer in open-cellular porous materials at high temperatures. In *Cellular and Porous Material Thermal Properties Simulation Prediction*; Wiley-VCH: Weinheim, Germany, 2008; pp. 165–198.
55. Coquard, R.; Loretz, M.; Baillis, D. Conductive heat transfer in metallic/ceramic open-cell foams. *Adv. Eng. Mater.* **2008**, *10*, 323–337.
56. Bhattacharya, A.; Calmidi, V.V.; Mahajan, R.L. An analytical-experimental study for the determination of the effective thermal conductivity of high porosity fibrous foams. *ASME Appl. Mech. Divis. Publ. AMD* **1999**, *233*, 13–20.



57. Boomsma, K.; Poulikakos, D. On the effective thermal conductivity of a three-dimensionally structured fluid-saturated metal foam. *Int. J. Heat Mass Transf.* **2001**, *44*, 827–836.
58. Hamilton, R.L.; Crosser, O.K. Thermal conductivity of heterogeneous two-component systems. *Ind. Eng. Chem. Fundam.* **1962**, *1*, 187–191.
59. Miller, M.N. Bounds for effective electrical, thermal, and magnetic properties of heterogeneous materials. *J. Math. Phys.* **1969**, *10*, 1988–2004.
60. Calmidi, V.V.; Mahajan, R.L. The effective thermal conductivity of high porosity fibrous metal foams. *J. Heat Transf.* **1999**, *121*, 466–471.
61. Matsushita, M.; Monde, M.; Mitsutake, Y. Predictive calculation of the effective thermal conductivity in a metal hydride packed bed. *Int. J. Hydrog. Energy* **2014**, *39*, 9718–9725.
62. Dul’Nev, G.N.; Zarichnyak, Y.P. A study of the generalized conductivity coefficients in heterogeneous systems. *Heat Transf. Sov. Res.* **1970**, *2*, 89–107.

© 2014 by the authors; licensee MDPI, Basel, Switzerland. This article is an open access article distributed under the terms and conditions of the Creative Commons Attribution license (<http://creativecommons.org/licenses/by/4.0/>).